Towards the Upper-Ocean Unbalanced Submesoscale Motions in the *Oleander* Observations

HAIJIN CAO,[a,b] BAYLOR FOX-KEMPER,[c] ZHIYOU JING,[d] XIANGZHOU SONG,[a,b] AND YUYI LIU[d]

[a] *Key Laboratory of Marine Hazards Forecasting, Ministry of Natural Resources, Hohai University, Nanjing, China*
[b] *College of Oceanography, Hohai University, Nanjing, China*
[c] *Department of Earth, Environmental, and Planetary Sciences, Brown University, Providence, Rhode Island*
[d] *State Key Laboratory of Tropical Oceanography, South China Sea Institute of Oceanology, Chinese Academy of Sciences, Guangzhou, China*

(Manuscript received 24 June 2022, in final form 10 January 2023)

ABSTRACT: Oceanic submesoscale dynamics with horizontal scales < 20 km have similar temporal and spatial scales as internal gravity waves (IGWs), but they differ dynamically and have distinct impacts on the ocean. Separating unbalanced submesoscale motions (USMs), quasi-balanced submesoscale motions (QBMs), and IGWs in observations remains a great challenge. Based on the wave–vortex decomposition and the vertical scale separation approach for distinguishing IGWs and USMs, the long-term repeat *Oleander* observations in the Gulf Stream region provide an opportunity to quantify these processes separately. Here in this study, the role of USMs in the divergence is emphasized, which has confounded the wave–vortex decomposition of wintertime data in previous analyses. We also adopt the vertical filtering approach to identify the USMs by applying a high-pass filter to the vertical scales, as USMs are characterized by smaller vertical scales. This approach is tested with submesoscale-permitting model data to confirm its effectiveness in filtering the submesoscale velocity perturbations, before being applied to the compiled velocity data of the *Oleander* dataset (years 2005–18). The results show that the averaged submesoscale eddy kinetic energy by USMs can reach $\sim 1 \times 10^{-3}$ m^2 s^{-2} at $z = -30$ m in winter, much stronger than found in other seasons. Importantly, this study exemplifies the possibility of obtaining USMs from existing ADCP observations and reveals the seasonal dynamical regimes for the submesoscales.

KEYWORDS: Ageostrophic circulations; Eddies; Ocean dynamics; Small scale processes

1. Introduction

The oceanic motions over a wide range of scales result from a balance between atmospheric forcing and dissipation. Mesoscale turbulence in the form of cyclonic and anticyclonic eddies is responsible for approximately 80% of kinetic energy (Ferrari and Wunsch 2009) and can now be well identified by satellite altimetry (Morrow and Le Traon 2012). However, at smaller scales, several studies have pointed to internal waves (Müller et al. 2015; Torres et al. 2018; Cao et al. 2019) and submesoscale dynamics (e.g., Capet et al. 2008; Gula et al. 2014; Cao and Jing 2022) as potential regimes for the failure of geostrophic balance. These two classes of motions differ in efficiency and mode of transporting tracers, such as vertical heat flux (Su et al. 2020; Torres et al. 2022). Determining the primary dynamical regime is a crucial step in understanding the pathways by which energy is transferred from sources to sinks (Cao et al. 2021) and the statistical distribution of those sources and sinks (Pearson and Fox-Kemper 2018). In addition, different classes of motions must be handled differently during interpretation of future high-resolution satellite altimeter measurements, e.g., the forthcoming Surface Water and Ocean Topography (SWOT) mission (Morrow et al. 2019).

A central question is how strong internal waves are relative to quasi-balanced motions (nearly geostrophic flows characterized by small surface divergence) and unbalanced submesoscale flows (ageostrophic flows characterized by strong surface divergence) (e.g., D'Asaro et al. 2018); their relative intensities are not well known in most of the global oceans. High-pass filters in time or horizontal space are frequently employed to separate submesoscale motions from larger-scale processes (e.g., Cao et al. 2021), but it is challenging isolate the submesoscales as their scales vary (Dong et al. 2020, 2021; Bodner et al. 2023) and often overlap with internal gravity waves (Torres et al. 2018). It is expected that the mesoscales are dominated by quasi-balanced motions (QBMs), while the submesoscale range is composed of both unbalanced submesoscale motions (USMs) and internal gravity waves (IGWs). This division of the submesoscales is rarely investigated, but the intensities of both are expected to depend on the season, hemisphere, mesoscale eddy kinetic energy (EKE), and climate events (D'Asaro et al. 1995). Here USMs include highly nonlinear processes with typical ageostrophic, convergent features in the mixed layer (ML) (e.g., frontogenesis and ML instabilities: McWilliams 2016; D'Asaro et al. 2018). The USMs have $O(1)$ Rossby and Richardson numbers (Thomas et al. 2008), with horizontal scales usually smaller than 20 km and time scales from hours to days, resembling the scales of submesoscale instabilities and turbulence-arrested fronts (Dong et al. 2020, 2021; Bodner et al. 2023).

However, separating these motions in observations is a challenge because of the complex regimes and limited observations.

Supplemental information related to this paper is available at the Journals Online website: https://doi.org/10.1175/JPO-D-22-0134.s1.

Corresponding author: Haijin Cao, h.cao@hhu.edu.cn

DOI: 10.1175/JPO-D-22-0134.1

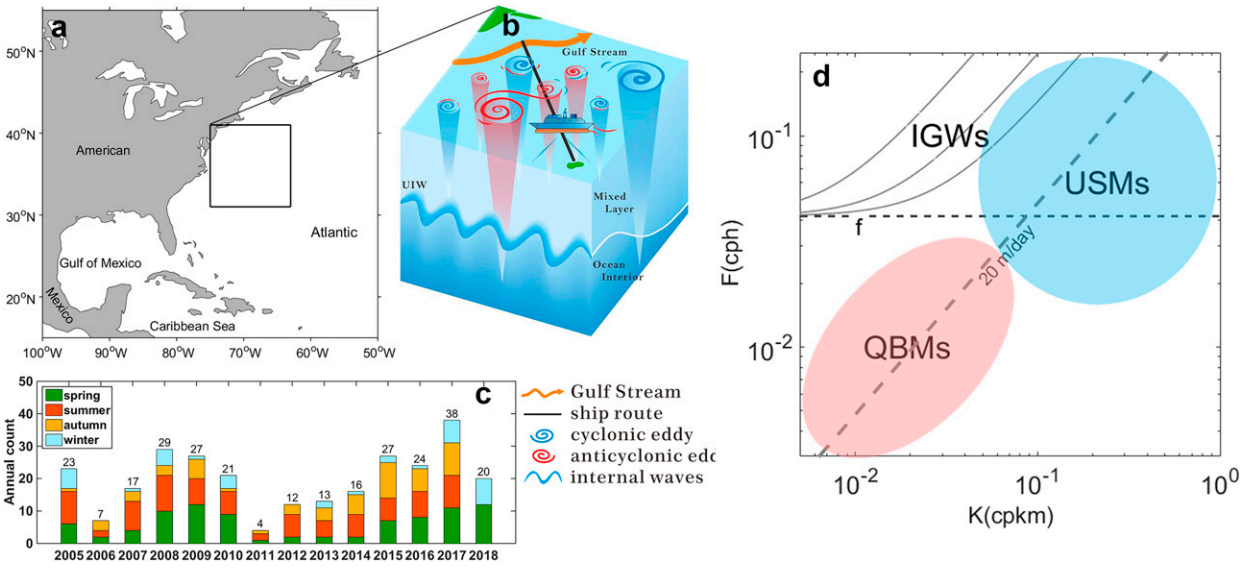

FIG. 1. (a) The study region indicated by the solid box. (b) Schematic diagram that illustrates the regional dynamical regimes: the mean flow (Gulf Stream), mesoscale/submesoscale eddies, and internal waves. The cruise track is also marked by the black line. (c) The annual count of data samples used in this study is divided into four seasons: spring (April–June), summer (July–September), autumn (October–December), and winter (January–March). (d) Schematic spectrum indicating the time and space scale of the three classes of motions.

Recently, a one-dimensional Helmholtz decomposition method was developed to separate divergent and rotational motions for stationary, homogeneous, and isotropic flows (Bühler et al. 2014). This method can further separate IGWs (with a prescribed combination of horizontally divergent and rotational motions) from the QBMs (purely rotational motions) in observations and has inspired many groups to reevaluate observations and models (Callies and Ferrari 2013; Callies et al. 2015; Rocha et al. 2016a; Qiu et al. 2017; Cao et al. 2019). In the Gulf Stream region, mesoscale eddies are active and the EKE varies seasonally (Zhai et al. 2008), while frequent storms or hurricanes may force the near-inertial motions (Alford 2003). Model-based studies (e.g., Torres et al. 2018) do not often separate the eddy or wave motions, so here the goal is to estimate the seasonally different KE contributions from QBMs, IGWs, and USMs by using both vertical filtering and the Helmholtz decomposition.

Repeat shipboard acoustic Doppler current profiler (ADCP) measurements over 14 years (2005–18) from the *Oleander* project collect the along-track flow velocity capturing the mesoscale and submesoscale currents in the upper ocean. Spectral study of the first decade of these data concluded that USMs are not very energetic in this region, dominating only on scales near 20 km and smaller, but due to the limited *Oleander* record at that time seasonal variations were disregarded (e.g., Callies and Ferrari 2013). A later study by the group (Callies et al. 2015) addressed seasonality, but did not distinguish between USMs and IGWs. Indeed, the Bühler et al. (2014) decomposition amounts to the assumption of wave dominance in the divergent component, which may be violated in the presence of strong USMs. This may cause misunderstanding of the dynamical regimes for the submesoscales. So we first revisit the observations by investigating the transition from quasi-balanced, nearly geostrophic flows to IGWs/USMs and its variability over seasons following Bühler et al. (2014). Afterward, we further separate USMs from IGWs by applying a high-pass filter to the vertical scales in the weakly stratified layers (Torres et al. 2022). This approach actualizes the assumption that USMs are characterized by smaller vertical scales, e.g., those typical of the stratification anomalies within the mixed layer itself (Fox-Kemper et al. 2008; Thomas et al. 2008). By contrast, the IGWs that have horizontal and temporal scales falling within the submesoscale range tend to have larger vertical scales. In this way, we isolate the USMs quantitatively from the velocity profiles of the *Oleander* ADCP observations. The results demonstrate that the submesoscales are dominated by USMs rather than by IGWs during wintertime, while the opposite is true during summertime.

2. Data and methodology

a. *The* Oleander *data*

The shipboard ADCP velocities on the *Oleander* have been collected for decades by this container vessel as it regularly transits the line between New Jersey and Bermuda (Figs. 1a,b) (Flagg et al. 1998). These repeat, long-term measurements have been used for many oceanographic studies (e.g., Wang et al. 2010; Rossby et al. 2014; Callies et al. 2015) and the fast-tow assumption has also been validated (e.g., Rocha et al. 2016a; Qiu et al. 2017). Here the along-track velocity data from 2005 to 2018 as collected by a hull-mounted 75-kHz Ocean Surveyor ADCP were block averaged over into 5-min bins, and then these data were interpolated onto a 2.5-km regular grid (available from the archive http://po.msrc.sunysb.edu/Oleander/). In this study, data at depths of 30 and 220 m are primarily used, representing the ML and pycnocline, respectively. The data are guaranteed to be high quality up to depths of ~220 m.

To examine seasonality, the data are categorized into four seasons: spring (April–June), summer (July–September), autumn (October–December), and winter (January–March). The number of cruises for each year by season is shown in Fig. 1c. To avoid including the Gulf Stream (Fig. 1b), only transects to the east of 70°W and the south of 35°N and with a continuous length of 300 km are used in this study (278 sections in total). The observed velocity includes dominantly subinertial flows, IGWs, and USMs. These classes of motions dominate different spectral spaces: quasi-balanced motions (QBMs) at low frequencies and low wavenumbers, USMs at high frequencies and high wavenumbers, and IGWs roughly along the dispersion relation curves associated with their vertical modes (Fig. 1d). The analysis shows that typically two or three mechanisms govern upper-ocean dynamics in this region, and which dominate changes seasonally with ML depth, stratification, and surface forcing. When all three mechanisms are present is the most complex situation analyzed. In that case, filtering of both time and space scales (frequency–wavenumber spectrum) is often used to separate these classes of motions for model data (e.g., Cao et al. 2021) but is impracticable for these shipboard ADCP data.

b. *The llc4320 MITgcm data*

The llc4320 MITgcm data are employed in this study. The llc4320 (refers to latitude–longitude–polar cap) is a global ocean simulation with a nominal grid spacing of 1/48° (~2 km) and 90 vertical levels (Forget et al. 2015). The simulation includes 16 tidal constituents (inadvertently overestimated by a factor of 1.1121; Uchida et al. 2022), and the 6-hourly atmospheric forcing from the European Center for Medium-Range Weather Forecasts atmospheric operational model analysis was used as surface boundary conditions. With this resolution and forcing, this model resolves most of the low-vertical-mode IGWs and a portion of USMs in the Gulf Stream region (Dong et al. 2020, 2021). The tenth baroclinic vertical mode is almost the highest baroclinic mode resolved in the simulation (Torres et al. 2018). This model has been widely used to study submesoscale processes over global oceans (e.g., Rocha et al. 2016a,b; Savage et al. 2017; Qiu et al. 2018; Torres et al. 2018; Cao et al. 2019; Dong et al. 2020, 2021). Here the model output is employed to test the method of filtering USMs by separating variability according to vertical scales.

c. *1D wave–vortex decomposition*

The 1D decomposition developed by Bühler et al. (2014) assumes stationarity, homogeneity, horizontal isotropy of the flow, and that all divergence is attributable to wave motions, which are not always good assumptions (Cao et al. 2019; Pearson et al. 2020). Nevertheless, to proceed we first continue with these assumptions and then revisit the uncertainty they imply following Cao et al. (2019). To begin, the velocities are rotated into the along-track (u) and across-track (v) velocity with the x axis aligned with the ship track before spectral decomposition. The 1D velocity spectra (S_u and S_v) are first obtained through the discrete Fourier transform. Data segments with 50% overlap and a 300-km tapering (Hanning) window were used to remove broadband bias and variance in these spectral estimates. The Helmholtz decomposition, $S = S_u + S_v = S^{\psi} + S^{\phi}$, requires ensemble estimates of the power spectra, with S_u the along-track velocity spectrum, S_v the across-track velocity spectrum, S^{ψ} the rotational spectrum, and S^{ϕ} the divergent spectrum. By assuming the Garrett–Munk spectrum (Munk 1981) for internal waves and wave dominance of the divergence (rather than in combination with USMs divergence), the wave–vortex decomposition is obtained $S = S_u + S_v = S_V + S_W$ (see the online supplemental material file for detailed derivation). To clarify that USMs may be confounding the wave diagnosis, we will refer to the waves diagnosed in this manner as "apparent waves." Note that violations of these basic assumptions in effect limit the accuracy of the decomposition, but the Bühler et al. (2014) method is the unique extant approach to assess the importance of balanced flows versus unbalanced motions from observations of the type collected by the *Oleander* ADCP. Here we use the error estimate on the decomposition assumptions developed in Cao et al. (2019) to quantify the limits of the method and avoid overinterpretation. The assumptions are approximately true for the scale range investigated in this study (<20 km), as the Gulf Stream is chopped off from the data analyzed which strongly reduces the potential for flow anisotropy.

3. Seasonal spectral decomposition

The averaged along-track and across-track velocity spectra for the 30-m layer (ML, solid) and 220-m layer (pycnocline, dashed) are plotted in Fig. 2. The ML exhibits much more energetic mesoscale flows than the deep, while the two layers display a similar KE level at the submesoscales in most seasons except for autumn. At the 220-m layer, submesoscale dynamics are expected to be weak because that layer is almost below the mixed layer in all seasons. Even during summertime, the submesoscale KE appears to be less depth dependent compared to the mesoscale KE (Fig. 2). A likely interpretation for the summertime strong KE over the scale range of 5–30 km is due to IGWs in the stratified layer, as also inferred by Callies et al. (2015). Also, it is important to make sure that the submesoscales are not dominated by the ADCP noise. Here the 95% confidence interval is taken as the errors to validate whether the noise spectrum would rival the true spectrum (see the supplemental material file for details). The prominent seasonal difference of submesoscale KE can also be taken as evidence of the clear spectrum (i.e., if the noise dominates the submesoscale spectrum, there should be no difference between seasons).

Figure 3 shows the spectra decomposed into vortex and apparent wave components using the Bühler et al. (2014) method: S_V and S_W at 30- and 220-m depths. An estimate of the errors due to assuming homogeneous and isotropic flows following Cao et al. (2019) suggests that the separation between the apparent wave and vortex contributions of the decomposition is trustworthy here (see the supplemental material file). Classifying the data into four seasons allows an examination of the seasonal difference between vortex and apparent wave components. Within the ML, the vortex component dominates the KE

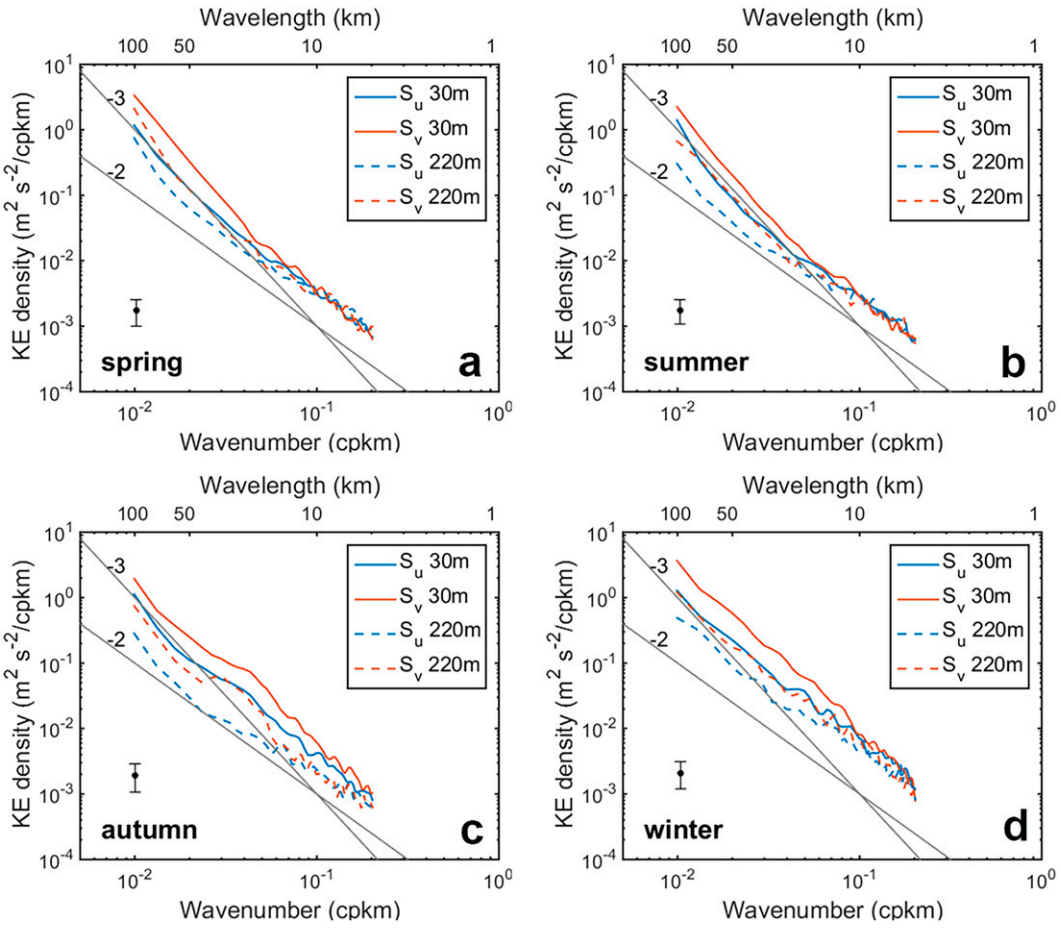

FIG. 2. Averaged along-track (blue) and across-track (brown) velocity wavenumber spectra in four seasons: (a) spring, (b) summer, (c) autumn, and (d) winter. The solid lines are for the 30-m layer, and the dashed lines are for the 220-m layer. The k^{-2} and k^{-3} power lines are marked in gray for reference.

with the spectra sloping down approximately along a k^{-3} power law in all seasons (consistent with the geostrophic prediction), before being taken over by apparent wave components. At the 30-m layer, the vortex-to-apparent wave transition occurs at scales near 20 km during spring and summer and below 10 km during autumn and winter. Note that the wintertime vortex components show a sloping trend between the k^{-3} and k^{-2} power law across the mesoscale and submesoscale range (Fig. 3d). The shallower spectral slope than the geostrophic expectation gives pause to the typical interpretation because of strong submesoscale dynamics, and submesoscales may reach quite large scales because of the deep ML in wintertime and the proportionality between ML depth and submesoscale lateral scale (Dong et al. 2020). Also, note that the wintertime apparent wave energy appears to be significantly enhanced at the submesoscales over the 5–25-km range (Fig. 3d), which implies either waves or strong submesoscale USM turbulence. At the 220-m layer, the KE spectra show a clear decrease at the mesoscale but not at the submesoscale, as evidence for strong submesoscale turbulence below the ML. As above mentioned, the submesoscale turbulence at depth arises mostly from IGWs, as an explanation for the increased transition scale in all seasons.

In summer, this apparent wave–vortex decomposition is credible as a wave–vortex decomposition because the summertime submesoscale processes leading to vortex motions are relatively weak (Callies et al. 2015) or probably have smaller length scales (Dong et al. 2020) that cannot be well resolved here. But in the wintertime ML, the ageostrophic aspects of submesoscale eddies or fronts (i.e., USMs) may also importantly contribute to the divergent (apparent wave) components. This violates the assumption that horizontal divergence is fully attributable to IGWs in the Bühler et al. (2014) wave–vortex decomposition. If the assumption of wave dominance of divergence is erroneous, the alternative in the Bühler et al. (2014) approach of neglecting the divergence by submesoscale dynamics altogether would cause large errors for the decomposition. At this point, using the decomposition of Bühler et al. (2014) in winter requires some caveats about the interpretation of divergence, and section 5 provides these and concludes that wave contributions are overestimated by this method, especially during winter due to USM contributions.

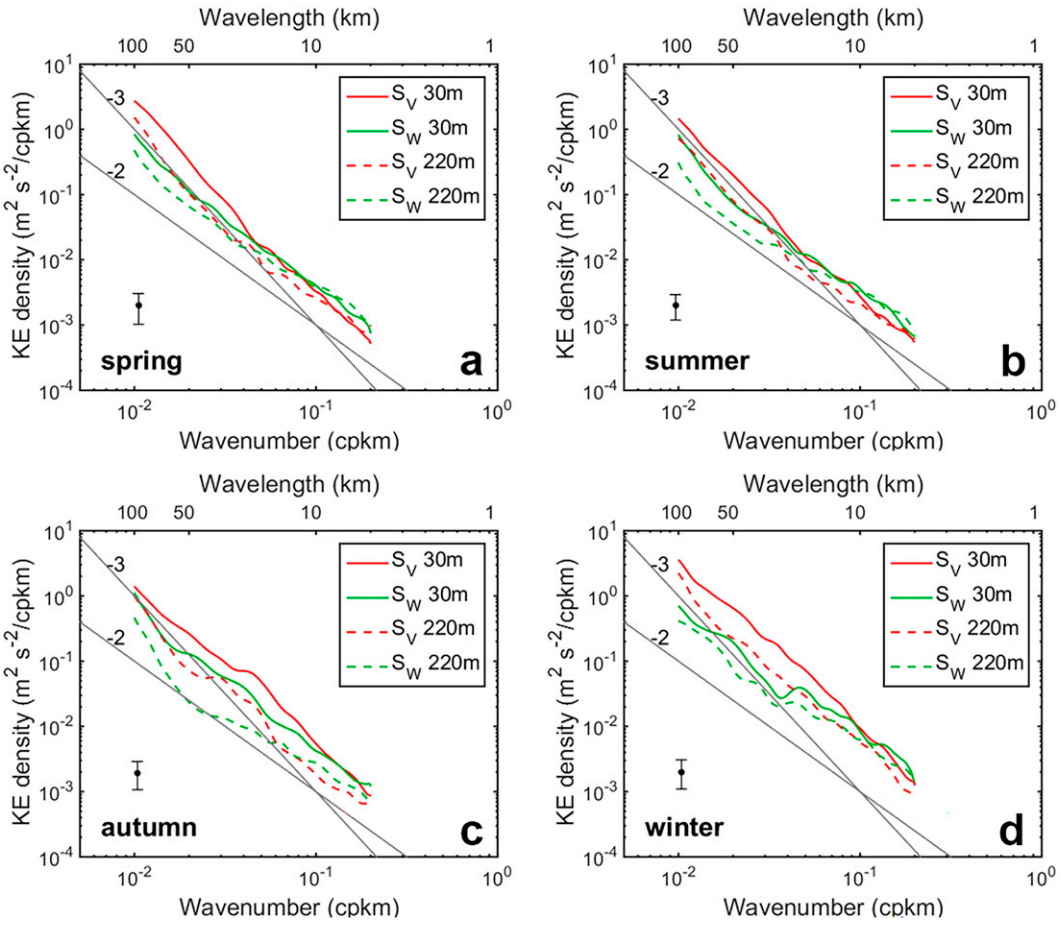

FIG. 3. Decomposed wavenumber spectra for vortex (red) and wave (green) parts in four seasons: (a) spring, (b) summer, (c) autumn, and (d) winter. The solid lines are for the 30-m layer, and the dashed lines are for the 220-m layer. The k^{-2} and k^{-3} power lines are marked in gray for reference.

4. Annual cycle of vortex and apparent wave dynamics

To gain more insight into the underlying regimes for the submesoscales, the annual cycle of vortex and apparent wave KE and the transition scale between them are examined (Fig. 4). Each year is not equally sampled by season (recall Fig. 1c) and as just presented remarkable seasonal differences exist, so averaging the data annually is unwise (i.e., violates the assumption of stationarity). Consider the cruises categorized by month in Fig. 4 to illustrate the annual cycle of the submesoscale vortex and wave KE and the transition between them. In this way, there can be sufficient data in each sample used to obtain accurate averaged spectra (the observations over more limited data bins would cause large errors in estimating the average spectra due to the highly variable year-to-year variations in decomposed KE).

IKE is defined as the kinetic energy found by integrating the spectra over a specified range of scales for comparison between time periods,

$$\mathrm{IKE}_V = \int_{k_1}^{k_2} \frac{1}{2} S_V dk, \quad \mathrm{IKE}_W = \int_{k_1}^{k_2} \frac{1}{2} S_W dk, \tag{1}$$

where k_1 and k_2 indicate the bounds of the wavenumber. Here the scales of 5–20 km are classified as submesoscales. The 5–20-km vortex and apparent wave IKE for the ML undergo a clear annual cycle, with peak values in February (Fig. 4a). The winter months show stronger submesoscale vortex turbulence than the summer months, especially in the ML. The vortex–apparent wave transition scales at 30-m depth stay below 10 km, indicating strong vortex contributions, except for June, July, August, and September (solid line in Fig. 4c). Despite the weaker (stronger) vortex and apparent wave IKE during near-summer (winter) months, the larger (smaller) transition scale occurs mostly because of the seasonal variation of vortex contributions. The reduction in vortex IKE is larger than the reduction in apparent wave IKE from winter to summer. It is also reasonable to infer that some of the wintertime unbalanced IKE could result from USMs, as they too contribute to horizontal divergence and thereby violate the assumed wave dominance of divergence in the wave–vortex decomposition. At the 220-m layer (Fig. 4b), the monthly variation of wave KE is not as prominent as that of the 30-m layer, and the wave component is stronger than the vortex

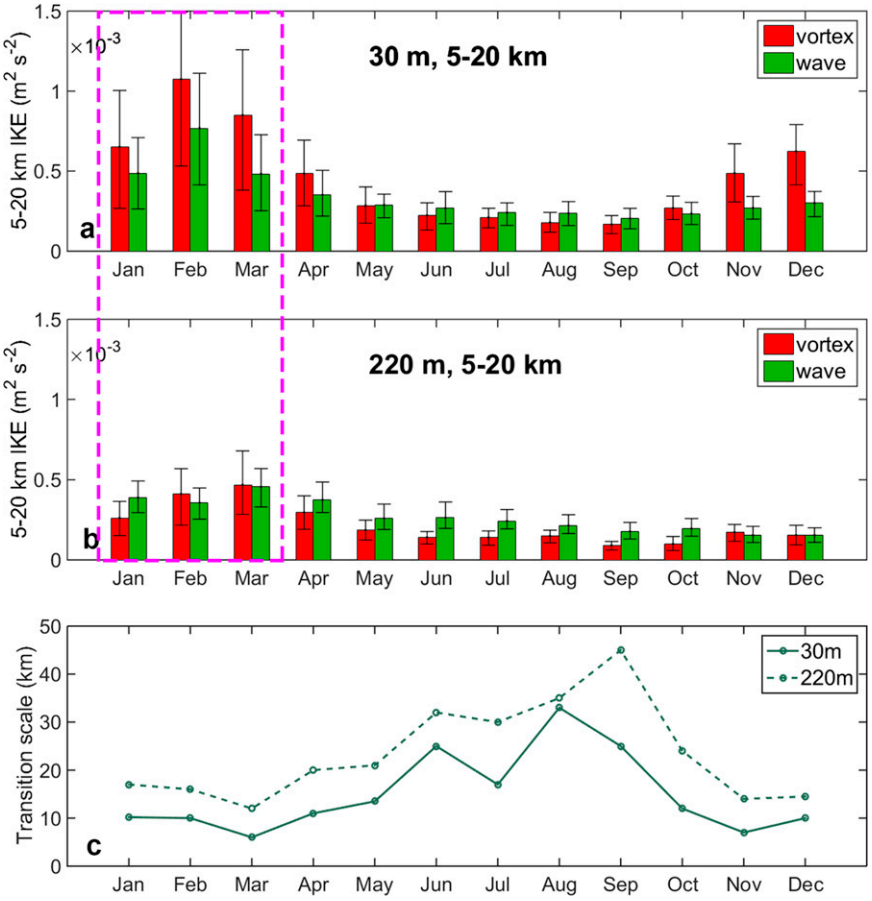

FIG. 4. Histograms of the vortex (red) and wave (green) 5–20-km integral kinetic energy (KE) at (a) 30 and (b) 220 m. (c) The transition scale between the vortex and wave component at 30 and 220 m. Here the transition scale is defined as the wavelength at which the mean wave component matches the mean vortex component. The magenta rectangle highlights the wintertime months when the decomposition may be ill-advised.

KE in most of the months. Thus, as expected the pycnocline submesoscales (here 5–20 km) are dominated by IGWs. The transition scale, where the spectral vortex component equals the apparent wave component, reaches ~46 km in September.

The difference in seasonality between the transition scale and IKE results from the fact that submesoscale dynamics and IGWs undergo out-of-phase seasonal cycles (Rocha et al. 2016b). In winter, the USMs become vigorous and may dominate submesoscale variability and the apparent wave contribution; while in summer, the strong seasonal pycnocline and shallow ML tend to strengthen the IGW dynamics contribution. The seasonal changes affect the transition scale between vortex and apparent wave components. In addition, the frequently encountered storms during summertime can also input wave energy that dominates the KE at the submesoscale in observations and models (e.g., D'Asaro et al. 1995; Alford et al. 2016), but it cannot be well identified from the *Oleander* data collected by shipboard ADCP alone. However, the apparent wave IKE does not show an increase in the summer months (Figs. 4a,b). One possible explanation is that the wintertime apparent wave component is mainly provided by USMs rather than by IGWs—as verified in the following sections.

5. Separating USMs by vertical filtering

a. Vertical-filtered analysis with the llc4320 model data

Although the contribution of USMs to divergence and vertical velocity is recognized (e.g., D'Asaro et al. 2018), it has not been considered easy to categorize the contributing phenomena, let alone separate USMs and IGWs in the submesoscale range. However, Torres et al. (2022) recommend a pragmatic approach to obtaining mainly USMs by removing any signals with low vertical modes (including IGWs and some QBMs). Here we choose two snapshots of the llc4320 data on 15 February (winter) and 15 August (summer) in the *Oleander* cruise region to illustrate this method. Note that this approach further assumes USMs are mostly trapped within the ML. This may be not true at the Gulf Stream front because submesoscale dynamics occur along the slanted isopycnals and thereby extend deeper than normal

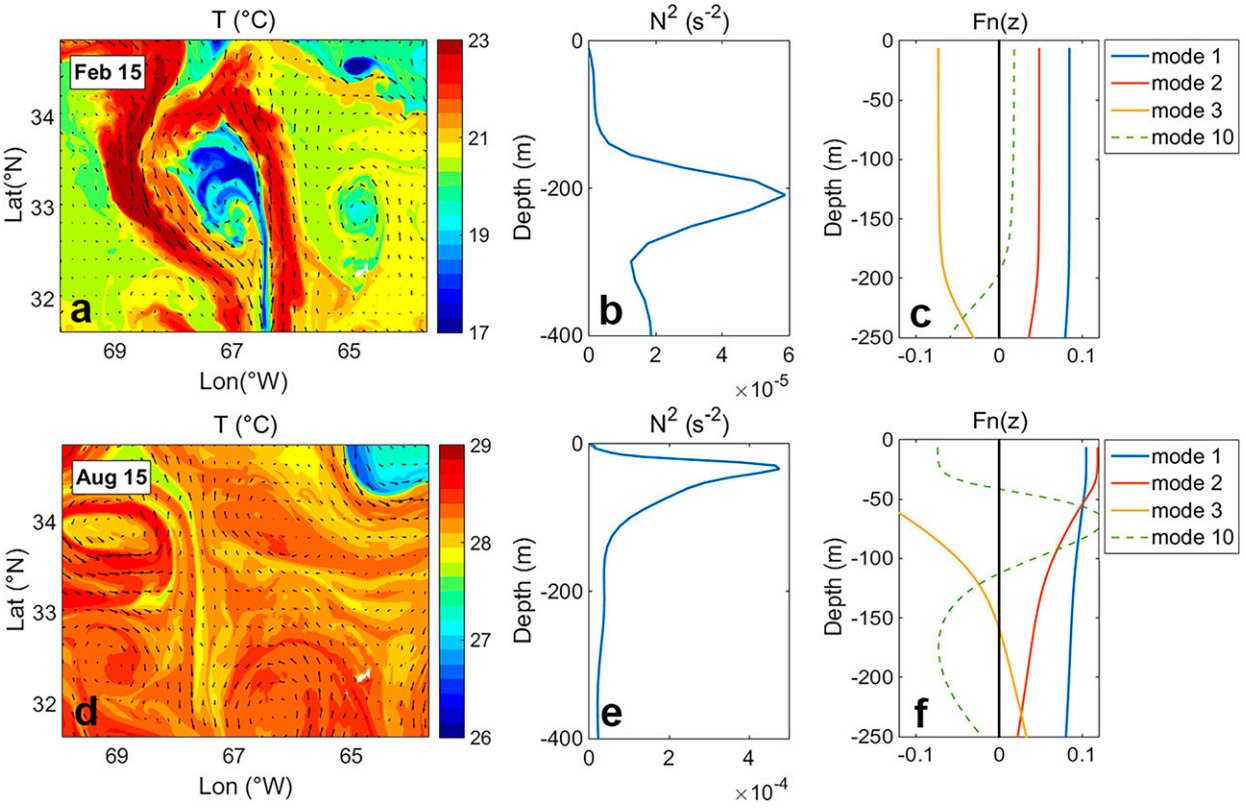

FIG. 5. Snapshots of surface temperature and velocity for (a) February and (d) August. (b),(e) Stratification averaged over the domains for the two snapshots. (c),(f) The vertical profiles of baroclinic modes (mode 1, 2, 3, and 10) for horizontal velocity for the two snapshots.

(Klymak et al. 2016; Cao and Jing 2022). So, in the model as well as observations we remove the Gulf Stream front and consider the region to the south of 35°N (Figs. 5a,d). Figures 5c and 5f show the eigenfunctions (F_n) of the vertical normal modes as obtained by solving a Sturm–Liouville problem (Gill 1982),

$$\frac{d}{dz}\left(\frac{f^2}{N^2}\frac{dF_n}{dz}\right) + \lambda_n^2 F_n = 0, \tag{2}$$

with $dF_n/dz = 0$ at $z = 0$ and $-H$. Here f is the Coriolis parameter, N^2 is the stratification, λ_n is the vertical eigenvalues, and H is the depth. In Eq. (2), the eigenvalue λ_n takes discrete, distinct values for each finite vertical scale H, so that the corresponding functions (F_n) form a set of eigenfunctions that are orthogonal and serve as a basis for the projection of variability into each mode. In this way, the vertical structure of each baroclinic mode is found. Expansion of the velocity on the vertical normal modes (u_l, v_l) can be written as

$$u_l = \sum_{n=0}^{\infty} u_n(x, y, t)F_n(z), \quad v_l = \sum_{n=0}^{\infty} v_n(x, y, t)F_n(z), \tag{3}$$

with $n = 0$ for the barotropic mode and $n > 0$ for the baroclinic modes. If the upper extent of n is limited, rather than infinite, then u_l and v_l represent the velocity associated with low modes. Figures 5b and 5c (Figs. 5e,f) display the averaged stratification and the eigenfunctions (F_n) for mode 1, 2, 3, and 10 in February (August). The results show that the zero-crossing points of the first 10 baroclinic modes (approximately corresponding to the highest baroclinic mode this simulation can resolve) occur below 200 m in February but only below 50 m in August. This reflects the evolving stratification between the winter and summer seasons. Since USMs are defined as highly nonlinear processes in the ML, they are likely to have much smaller horizontal and vertical scales than QBMs. This eigenmode analysis reveals the vertical structures of QBMs and IGWs are simple within the ML. By contrast, the velocity of USMs (u_{USMs}, v_{USMs}) is assumed to have a complex vertical structure within the ML. The velocity structures associated with the low modes (v_l, v_l)—i.e., the QBMs and IGWs can be approximated using only a linear trend (Figs. 5c,f). Removing a detected linear trend over the ML serves as vertical filtering of the vertical velocity profile. Here we take the zero-crossing depth of mode 10 as a threshold depth (z_t), which may be deeper than the ML. Then we can filter out the low-mode signal in the velocity field [Eq. (4)] by removing the linear trend between the surface and z_t. At each grid point (x, y), the velocity above z_t can be decomposed into the low-mode component (the first 10 baroclinic modes, each approximated by a linear trend) and the USMs component:

$$U = U_l + U_{\mathrm{USMs}}. \tag{4}$$

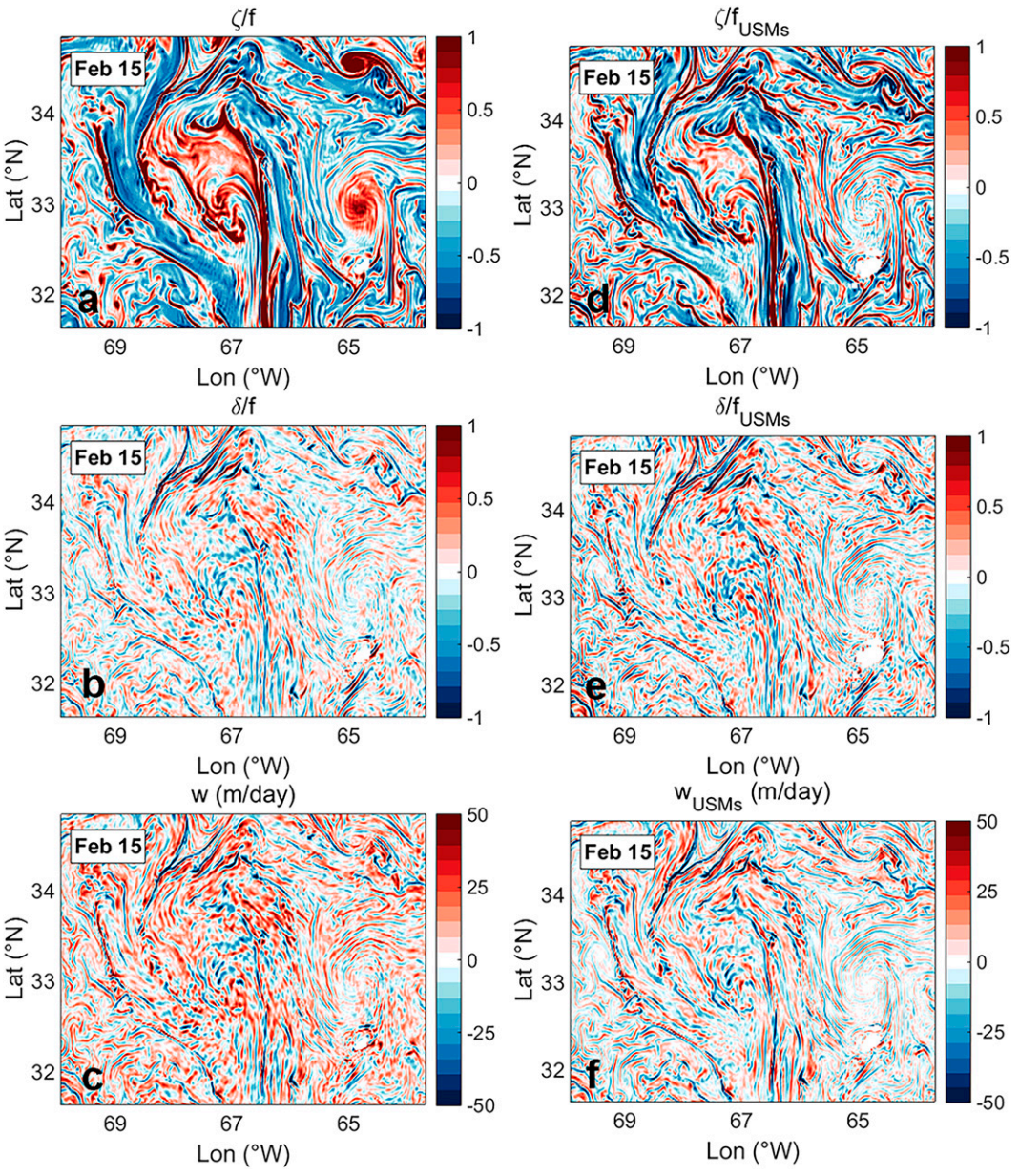

FIG. 6. Snapshots of (a),(d) vertical vorticity, (b),(e) horizontal divergence, and (c),(f) vertical velocity fields calculated with (left) unfiltered and (right) filtered data at $z = -10$ m for February.

In Eq. (4), U represents a velocity component and can be u or v. The low-mode velocity can be derived by estimating the linear trend in vertical, and thus the remaining is the velocity by USMs. The low-mode field can be written as

$$U_l = c_1 + c_2 z, \tag{5}$$

where both c_1 and c_2 are constant at each grid point. Most often the linear trend of u and v between the surface and z_t is weak with $u = u_l$ and $v = v_l$ at z_t, so a nearly uniform velocity between the surface and z_t is associated with the low-mode contribution. Equations (4) and (5) are also true for vertical velocity w. Consider the boundary conditions, $w_{\mathrm{USMs}} = 0$, at the surface and z_t to obtain $c_1 = w(0)$ and $c_2 = [w(z_t) - w(0)]/z_t$. This decomposition regards the USMs as signals with smaller vertical scales and shear within the weakly stratified ML, which conforms to the general definition of USMs (McWilliams 2016). According to the vertical extent of first through tenth normal modes (Figs. 5c,f), $z_t = -200$ and -50 m are defined as the fixed depths for vertical filtering in February and August, respectively. Choosing a slightly different threshold depth, e.g., -190 or -210 m for February, does not make a big difference in the USMs diagnosed.

To illustrate the USMs as thus diagnosed, Figs. 6 and 7 compare the unfiltered and filtered llc4320 simulated relative

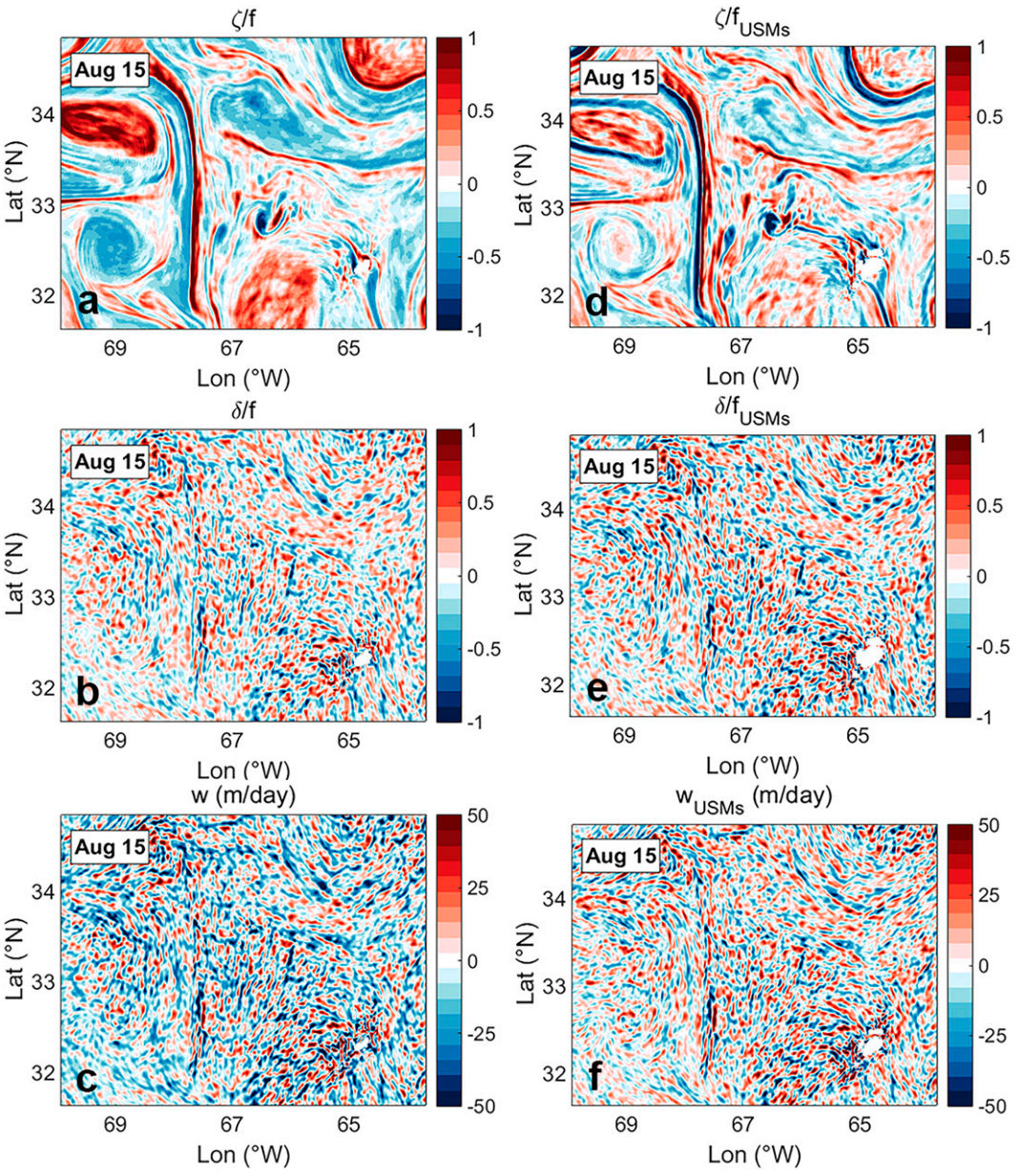

FIG. 7. As in Fig. 6, but for August.

vorticity (ζ), lateral divergence (δ), and vertical velocity (w) fields at $z = -10$ m in the two different seasons. Both ζ and δ are normalized by the local Coriolis frequency ($f = 8.04 \times 10^{-5}$ rad s^{-1}). The divergence is slightly smaller but still comparable in strength to the vorticity, consistent with the prediction of turbulent thermal wind balance (Gula et al. 2014; Dauhajre and McWilliams 2018). A comparison between the ζ/f fields before and after filtering illustrates that the large vorticity is mainly owing to submesoscale dynamics along fronts, which is likely associated with frontogenesis (Figs. 6a,d). The pairwise feature of cyclonic and anticyclonic streaks becomes more prominent in the filtered fields (Fig. 6d), indicative of the effectiveness of the filtering. Both the unfiltered and filtered δ/f fields (Figs. 6b,e) show a similar distribution compared to the ζ/f fields, indicating that the divergence is mainly dominated by USMs. The w field by USMs is relatively weak compared to the unfiltered w field (Fig. 6f compared to Fig. 6c) and is much more concentrated near fronts and filaments. The USM w can reach a maximum magnitude of ~50 m day^{-1} mainly at this depth, roughly corresponding to the distribution of the filtered ζ/f and δ/f fields. All these features suggest that the vertical filtering approach is effective in isolating USMs for the winter case. Although the USMs only take up a minor part of KE, with the majority of energy being associated with the low vertical modes (QBMs and IGWs) (see the supplemental material file), they cannot be ignored

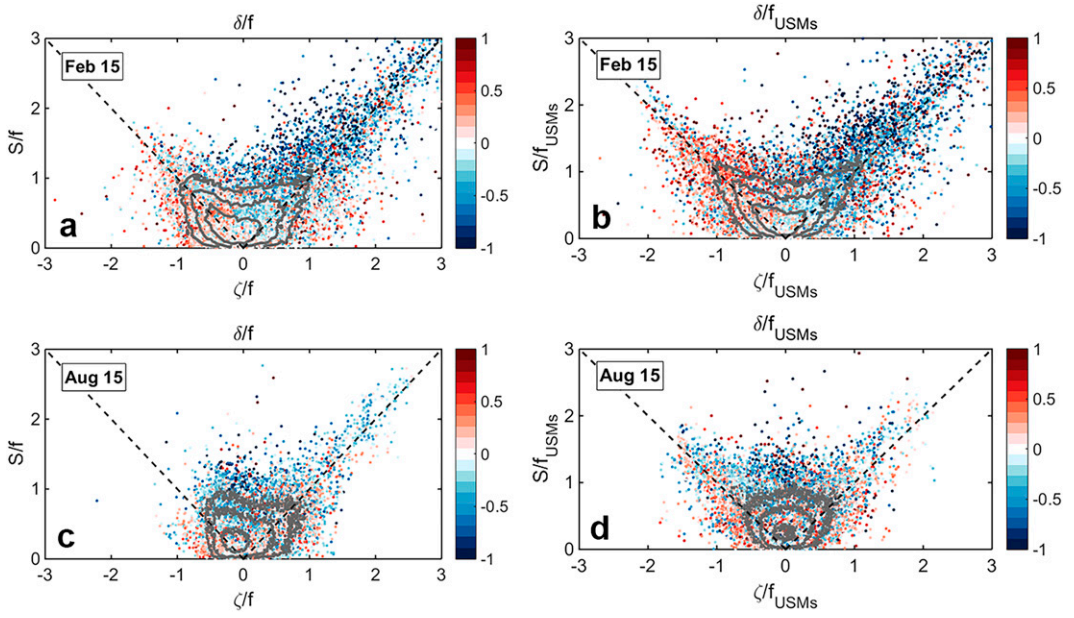

FIG. 8. Lateral divergence in vorticity–strain space for filtered and unfiltered velocity fields at $z = -10$ m. The dark contours indicate the joint probability distribution function of vorticity and strain. Conditioning the divergence on the vorticity and strain for (a),(b) February and (c),(d) August. The dashed lines divided the flow into the strain-dominated regime ($S > |\zeta|$) and eddy dominated regime in terms of the Okubo–Weiss parameter, $S^2 - \zeta^2$.

because of their importance in ML dynamics—the USMs play an important role in restratification, energy transfer and dissipation, and tracer exchange between the surface and the ocean interior (e.g., D'Asaro et al. 2011; Fox-Kemper et al. 2011; Su et al. 2018), with a horizontal convergence contribution outsized for their KE contribution (D'Asaro et al. 2018).

By contrast, the modeled USMs in summer are relatively weak (Fig. 7), which is most likely because the weaker buoyancy production due to the weaker buoyancy gradient in summer (Fig. 5d), as baroclinic conversion is important energy source for the submesoscales (Cao et al. 2021). Apart from that, the shallow ML in summer can limit the submesoscale energy conversion from available potential energy to kinetic energy and reduce the length scales of submesoscale instabilities leading to vortices to a few kilometers which are not well resolved in this simulation (Dong et al. 2020, 2021). The vorticity field is much weaker in summer (Fig. 7a), but it is surprising that the δ and w fields on 15 August (Figs. 7b,c) look as energetic as, or even a little more energetic than that on 15 February (Figs. 6b,c). Differently, the summertime δ and w fields show patterns of radial and crisscross beams resembling high-mode IGWs—note as shown in Fig. 5f that the relatively high vertical modes cross zero much closer to the surface in August due to the strong stratification. The different features between Figs. 7a and 7b (Figs. 7d and 7e) suggest that the divergence field is likely not dominated by submesoscale dynamics in summer. So the vertical filtering technique tends to be less effective in summer than in winter. It is also possible that the summertime USMs with smaller length scales are not well resolved in this simulation, which leads to an underestimate of USMs.

To better understand the relationship between vorticity and divergence fields, we further plotted the divergence/convergence in vorticity–strain space before and after the vertical filtering (Fig. 8). These scatterplots provide a statistical view of the filtered and unfiltered fields. Also, the Okubo–Weiss parameter, $S^2 - \zeta^2$, can be examined to identify the flow regime. In the winter case (Fig. 8a), the joint probability distribution function (JPDF) of vorticity and strain generally shows an extension along the $S = |\zeta|$ lines (shear flow), especially for cyclones (Balwada et al. 2021; Cao and Jing 2022). Conditioning divergence/convergence on vorticity and strain indicates that the strongest convergence mostly lies in the strain-dominated region ($S > |\zeta|$) driving frontogenesis at the near-surface layer (Fig. 8a), which is a typical feature of ML submesoscale dynamics (McWilliams 2017; Balwada et al. 2021). The strong divergence (red dots in Fig. 8a) mainly occurs in the $\zeta < 0$ region near the $S = -\zeta$ line. After removing the low-mode signals, the regime of strain-induced frontogenesis with strong convergence (McWilliams 2017) still exists (blue dots in Fig. 8b). However, the divergence tends to be more apparent in the $\zeta/f_{\mathrm{USMs}} < -1$ domain, making the JPDF less skewed (Fig. 8b), consistent with the pairwise distribution of large cyclonic and anticyclonic values in Fig. 6d. This feature is not expected in the traditional frontogenesis paradigm (McWilliams 2017), and it may be a trick of the filtering technique suggesting that the filtered USMs fields appear to be highly ageostrophic ($|\zeta/f_{\mathrm{USMs}}| > 1$). This is also likely ascribed to the interaction between submesoscale dynamics and IGWs at play, but here we will not look into the underlying dynamics and leave it to future studies. By contrast, The summertime JPDFs show a wider spreading with weaker ζ, δ, and

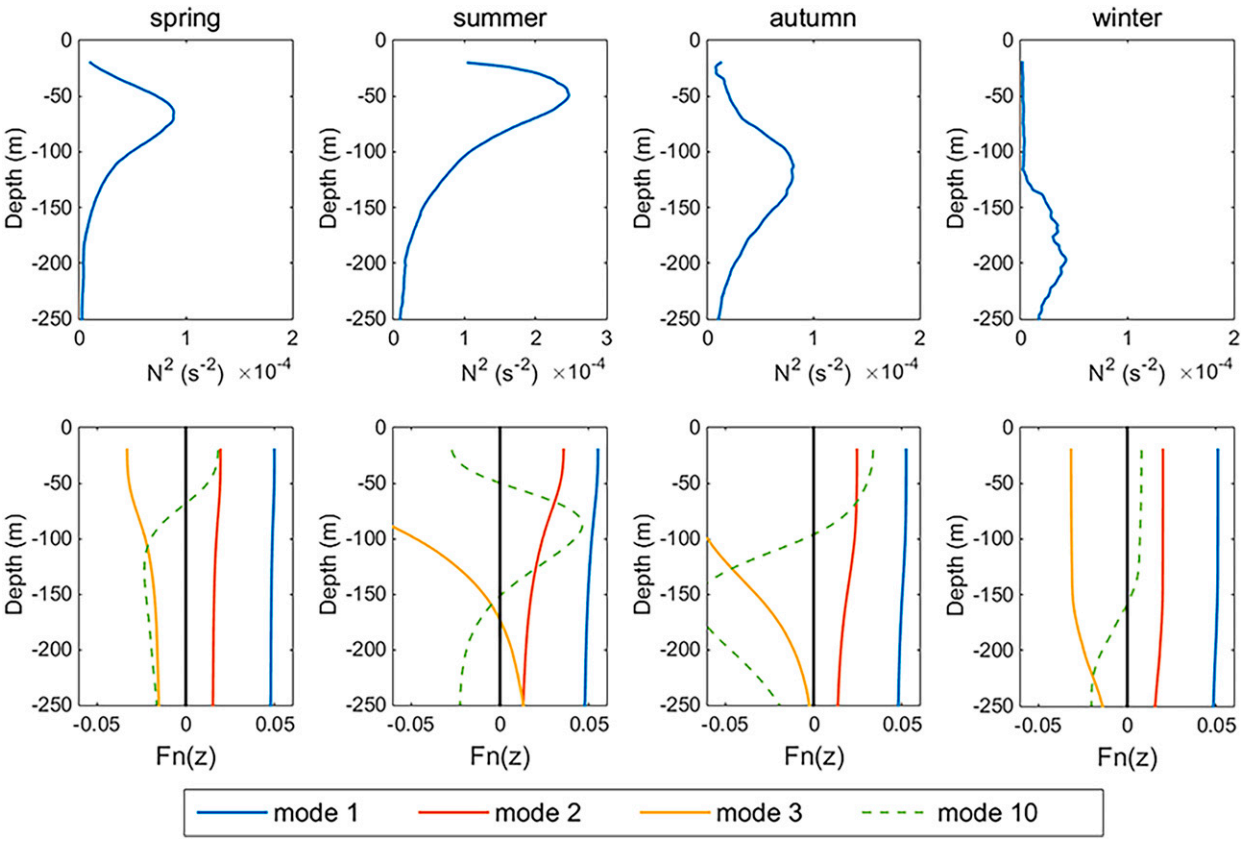

FIG. 9. (top) Upper-ocean stratification estimated along the ship route by season. (bottom) Vertical structure of baroclinic modes (mode 1, 2, 3, and 10) for horizontal velocity.

S in the vorticity–strain space (Figs. 8c,d), likely owing to the IGWs.

b. Vertical-filtered USMs analysis with the Oleander *data*

The *Oleander* shipboard ADCP data provide velocity profiles over the upper ocean, allowing the decomposition of the velocity field [Eq. (4)]. The seasonal stratification is estimated based on the *Oleander* XBT data and the Argo salinity data (Fig. 9, upper row). The vertical structure of the eigenfunctions (F_n) for the vertical normal modes (mode 1, 2, 3, and 10) are shown in Fig. 9 (bottom row) and thus z_t equals −75, −50, −100, and −150 m for spring, summer, autumn, and winter, respectively. Two example sections of KE and submesoscale EKE in February and August are presented (see the supplemental material file). In the winter case, the submesoscale EKE can be as strong as 0.01 $m^2\ s^{-2}$ much stronger than that of the summer case.

The separation of USMs by vertical filtering allows us to quantify the USMs in observations as exemplified in the model. The vertical distribution of the section-averaged submesoscale EKE is shown by season (Fig. 10). The USMs appear to be enhanced in the middle or at the base of the ML likely due to the enhancement of buoyancy production, consistent with the previous studies (Callies et al. 2015; Cao et al. 2021). The results also show that the submesoscale EKE displays clear seasonality with a peak in winter, as opposed to the summertime enhancement of mesoscale EKE (Zhai et al. 2008). The highest averaged submesoscale EKE during the wintertime reaches a magnitude of $\sim 1 \times 10^{-3}\ m^2\ s^{-2}$ in the ML. Indeed, this value is still one order of magnitude smaller than the mesoscale EKE which is estimated to be larger than $5 \times 10^{-2}\ m^2\ s^{-2}$ in the Gulf Stream region (Zhai et al. 2008). As discussed in Cao et al. (2021), the USMs come more from frontal dynamics (buoyancy production) rather than larger-scale flows (shear production), and this provides them with

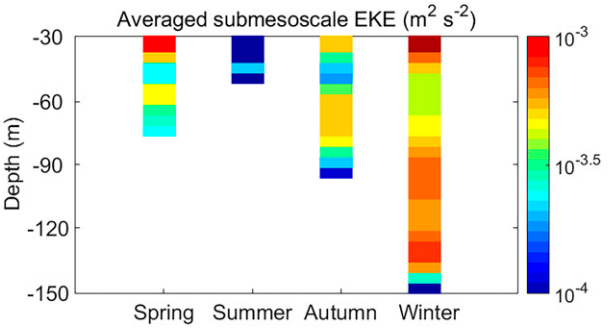

FIG. 10. Depth–season plot of the section-averaged submesoscale eddy kinetic energy (EKE; $m^2\ s^{-2}$).

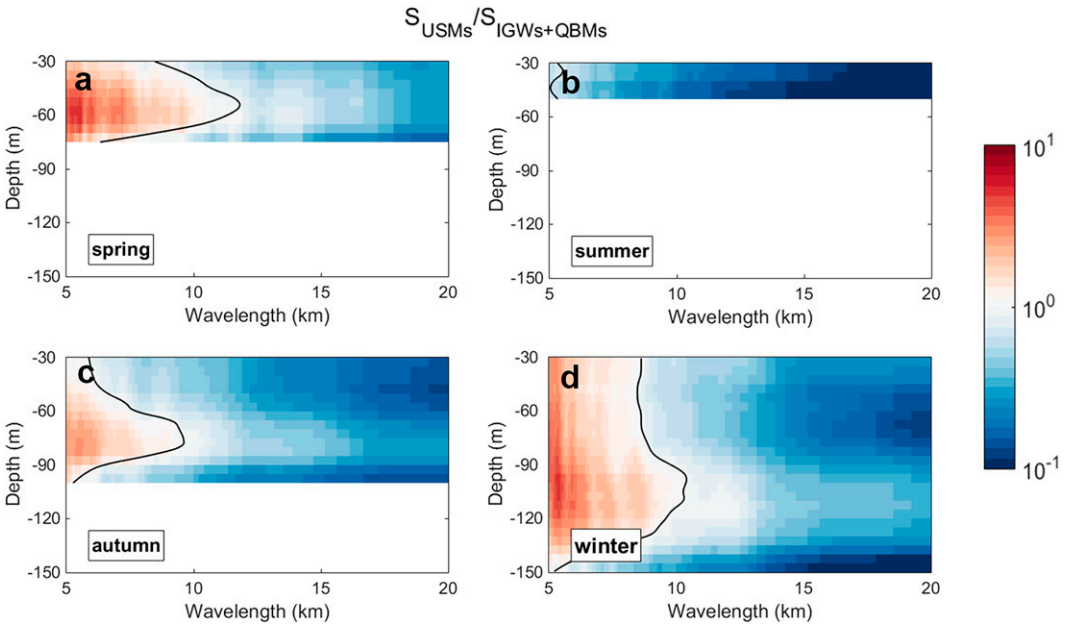

FIG. 11. The ratio of unbalanced submesoscale motions (USMs) over internal gravity waves and quasi-balanced motions (IGWs+QBMs) as a function of scales for (a) spring, (b) summer, (c) autumn, and (d) winter. A ratio larger than 1 (red shading) indicates the wavelengths dominated by USMs. The black line indicates the wavelengths where the spectral ratio $S_{USMs}/S_{IGWs+QBMs} = 1$ for different depths.

seasonality (Uchida et al. 2017). Besides, the shallow ML in summer also shrinks the scale of submesoscale processes, reducing their detection under fixed resolution. Note that the shallowest layer of the data is −30 m—during summertime submesoscales may be even closer to the surface and mostly not observed. As such, the validity of the summertime results is uncertain.

By comparing the spectra of S_{USMs} and $S_{IGWs+QBMs}$ by season, we can illustrate the effects of vertical filtering (see the supplemental material file) and then show the spectral ratios between the USMs and the remaining flow ($S_{USMs}/S_{IGWs+QBMs}$) to identify the length scales dominated by USMs in the upper ocean (Fig. 11). Here the black lines indicate the wavelengths where the USMs match the remaining motions in spectral space. Figure 11 shows that the wintertime USMs mostly dominate the submesoscales smaller than 10 km ($S_{USMs}/S_{IGWs+QBMs} > 1$) while the summertime USMs are relatively weak. Given that USMs also contribute to the divergence, the assumption of all divergence by wave motions in the Bühler et al. (2014) method is invalid in the ML with strong USMs. So the wave–vortex decomposition used in the first sections of this paper overestimated the wave EKE at scales where USMs are remarkable, especially in winter (recall Fig. 3d). The winter has stronger lateral buoyancy gradients for low baroclinic modes (Fig. 5a) that can generate QBMs, which explains part of the large vortex KE in the winter months (Fig. 4), but strong USMs also contribute to both the vortex and wave KE.

To evaluate further these claims, we conduct the wave–vortex decomposition on the low-mode flow (i.e., after USMs are removed) for the winter months and compared the wave and vortex components to the unfiltered results (Fig. 12a). Here we choose the 100-m layer, which has strong USMs, to illustrate the difference. After removing USMs, both wave and vortex spectra show a clear decrease for the submesoscales but remain almost unchanged for the larger scales. The wave IKE for the winter months is significantly reduced, while it is much less for the vortex IKE (Figs. 12b,c). This directly manifests the importance of USMs to the divergence field, demonstrating that the wave component will be overestimated in the Bühler et al. (2014) decomposition for winter if not removing the USMs. Although here the vertical filtering, depth range, and horizontal resolution (~2.5 km) are limited by the instrumental record and processing, it can be concluded that the USMs can exert a significant impact on the apparent wave–vortex decomposition of the winter data in the upper ocean of this region. On the contrary, the relatively weak USMs over 5–20 km in summer (Fig. 11b) do not significantly affect the decomposition.

6. Summary and discussion

The focus of this work is to understand the phenomenology and underlying regimes of the submesoscales captured in the *Oleander* ADCP velocity data. The decomposition of motions into geostrophic flows and IGWs reveals the seasonal contrasts of vortex and wave KE, and basic ranges of variability in vortex and wave components over months are quantified. However, important contributions from submesoscale USMs need to be handled separately, as they contain both vortical and divergent motions, but are not waves. We exemplify the vertical filtering approach to separating upper-ocean USMs in

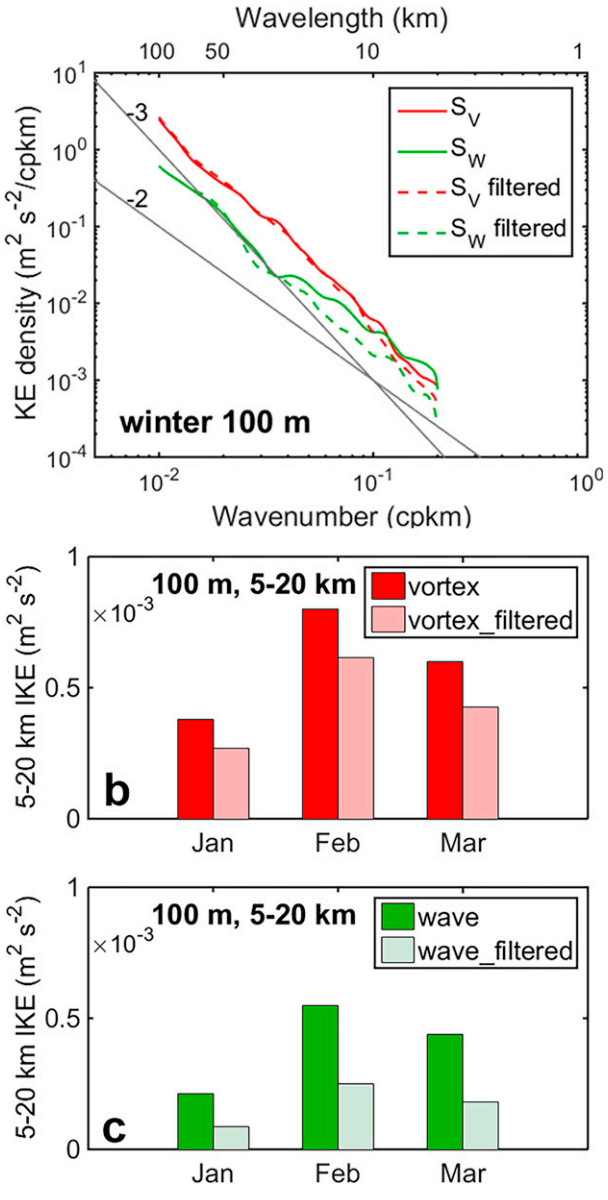

FIG. 12. (a) Comparison of wave–vortex decomposition on the unfiltered velocity (solid lines) and the filtered low-mode (QBMs+IGWs) contribution (dashed lines) for the wintertime 100-m layer. Shown also is the apparent reduction of (b) vortex and (c) wave IKE due to removal of USMs for the winter months.

observations. It is shown that USMs contribute meaningfully to divergence, especially in wintertime, and thus they spuriously confuse the wave–vortex decomposition of Bühler et al. (2014) unless they are removed first, e.g., by the pragmatic vertical filtering approach of Torres et al. (2022). The results provide a clear understanding of the seasonal dynamical regimes for the submesoscales (Table 1) and quantitatively evaluate the USMs from observations. It is concluded that in the upper ocean of the study region the submesoscales are primarily dominated by USMs in winter but by IGWs in summer. Importantly, this study opens the possibility of

TABLE 1. Seasonal dynamical regimes for the submesoscales inferred from the *Oleander* ADCP velocity data in the upper ocean.

	Spring	Summer	Autumn	Winter
−30 m	Transition	Mostly IGWs	Transition	USMs
−220 m	IGWs	IGWs	IGWs	Mostly IGWs

separating USMs from low-mode motions in existing ADCP observations.

The vertical filtering approach is effective in separating USMs and IGWs in individual observations where the dynamics are always aliased due to discrete sampling (e.g., shipboard ADCP data). However, this approach relies on the solution of eigenfunctions of vertical modes (with a threshold depth defined), which limits its application in summertime when the threshold depth is shallow and high-mode IGWs may exist. Our analyses also offer some caveats when interpreting the wave–vortex decomposition. The results confirm that the strong wintertime USMs dominate the submesoscale in the ML, and here we demonstrate that the horizontal divergence can come from either IGWs or USMs (recall Fig. 12). This violates the Bühler et al. (2014) assumption that IGWs are the dominant cause of divergence and causes large errors for the decomposition when applied at submesoscales, particularly in wintertime. So, in regions of strong USMs, the wave–vortex transition and estimated IKE for waves are not reliable during wintertime when submesoscale dynamics are sufficiently strong (e.g., the magenta rectangle in Fig. 4). The wintertime submesoscales in the ML are in fact dominated by vortex components at all length scales (i.e., there is no transition scale between QBMs and IGWs shown in Fig. 12a).

The assumption of waves dominating the divergence for the wave–vortex decomposition is strongly supported in this region during the summer at all depths examined. As such, the transition scale between vortex and wave components becomes much larger during summertime. This may be also partly attributed to the unpredictable storm events during summertime (e.g., Simmons and Alford 2012; Forryan et al. 2015). These storm impacts are generally missing or underestimated in numerical simulations due to limited resolution and frequency of forcing products (e.g., Tsujino et al. 2020, or in coupled atmospheres, Jochum et al. 2013) and give rise to great uncertainty in estimating IGWs in the ocean. We have shown here that nonwave submesoscale phenomena can also generate unbalanced motions and/or divergent motions, an effect resulting from the large Rossby number of the submesoscales and demonstrated elsewhere in models and observations of surface drifters (Fox-Kemper et al. 2008; D'Asaro et al. 2018). It is obvious at this stage that seasonal variations in forcing lead to the change of ML depth, which impacts the submesoscale response (e.g., Mensa et al. 2013; Sasaki et al. 2014; Dong et al. 2020; Zhang et al. 2020)—whether the surface synoptic variability, especially in storm-rich oceans, offers variable generation of submesoscale responses is another query to address (e.g., Chrysagi et al. 2021; Carpenter et al. 2020). It is also notable that another important issue—the

diurnal variability of submesoscale dynamics—is not considered in this study (see discussion in Sun et al. 2020).

Essentially, the USMs defined in this study are a typical reason for errors when reconstructing the upper-ocean circulation and interior structures based on assumed geostrophy, such as the surface quasigeostrophic (SQG) theory in the ML (e.g., Qiu et al. 2016; Chen et al. 2020). The reconstruction will be less effective when the ML is deep and strong USMs occur, unless the USMs are first separated from the normal low-mode vertical modes. Cautions should be taken when applying these methods in the circumstance of strong USMs. The many possible interactions between IGWs and USMs are not considered and could be another uncertainty for the analysis in this study. More numerical experiments with higher spatial resolution, realistic forcing, and nonhydrostatic physics are required to capture these smaller-scale processes and to better understand their dynamics and seasonality.

Acknowledgments. We thank the *Oleander* group for collecting and making available the data from long-term observations. We appreciate the efforts of and discussions with the *Oleander* team, especially Donohue and Rossby. We would also like to acknowledge the valuable comments and suggestions from the reviewers (Dr. Dhruv Balwada and another anonymous reviewer). This study is supported by the National Natural Science Foundation of China (42176004, 92058201, and 41776040). B. F-K. is supported by ONR N00014-17-1-2963 and NOAA NA19OAR4310366. Z. J. is partly supported by the Chinese Academy of Sciences (ZDBS-LY-DQC011).

Data availability statement. The *Oleander* ADCP data used in this study can be accessed at http://po.msrc.sunysb.edu/Oleander/. The llc4320 data can be accessed at https://data.nas.nasa.gov/ecco/. The Argo data are from https://argo.ucsd.edu/data/acknowledging-argo/ (http://doi.org/10.17882/42182).

REFERENCES

Alford, M. H., 2003: Improved global maps and 54-year history of wind-work on ocean inertial motions. *Geophys. Res. Lett.*, **30**, 1424, https://doi.org/10.1029/2002GL016614.

——, J. A. MacKinnon, H. L. Simmons, and J. D. Nash, 2016: Near-inertial internal gravity waves in the ocean. *Annu. Rev. Mar. Sci.*, **8**, 95–123, https://doi.org/10.1146/annurev-marine-010814-015746.

Balwada, D., Q. Xiao, S. Smith, R. Abernathey, and A. R. Gray, 2021: Vertical fluxes conditioned on vorticity and strain reveal submesoscale ventilation. *J. Phys. Oceanogr.*, **51**, 2883–2901, https://doi.org/10.1175/JPO-D-21-0016.1.

Bodner, A. S., B. Fox-Kemper, L. Johnson, L. P. Van Roekel, J. C. McWilliams, P. P. Sullivan, P. S. Hall, and J. Dong, 2023: Modifying the mixed layer eddy parameterization to include frontogenesis arrest by boundary layer turbulence. *J. Phys. Oceanogr.*, **53**, 323–339, https://doi.org/10.1175/JPO-D-21-0297.1.

Bühler, O., J. Callies, and R. Ferrari, 2014: Wave-vortex decomposition of one-dimensional ship-track data. *J. Fluid Mech.*, **756**, 1007–1026, https://doi.org/10.1017/jfm.2014.488.

Callies, J., and R. Ferrari, 2013: Interpreting energy and tracer spectra of upper-ocean turbulence in the submesoscale range (1–200 km). *J. Phys. Oceanogr.*, **43**, 2456–2474, https://doi.org/10.1175/JPO-D-13-063.1.

——, ——, J. M. Klymak, and J. Gula, 2015: Seasonality in submesoscale turbulence. *Nat. Commun.*, **6**, 6862, https://doi.org/10.1038/ncomms7862.

Cao, H., and Z. Jing, 2022: Submesoscale ageostrophic motions within and below the mixed layer of the northwestern Pacific Ocean. *J. Geophys. Res. Oceans*, **127**, e2021JC017812, https://doi.org/10.1029/2021JC017812.

——, ——, B. Fox-Kemper, T. Yan, and Y. Qi, 2019: Scale transition from geostrophic motions to internal waves in the northern South China Sea. *J. Geophys. Res. Oceans*, **124**, 9364–9383, https://doi.org/10.1029/2019JC015575.

——, B. Fox-Kemper, and Z. Jing, 2021: Submesoscale eddies in the upper-ocean of the Kuroshio Extension from high-resolution simulation: Energy budget. *J. Phys. Oceanogr.*, **51**, 2181–2201, https://doi.org/10.1175/JPO-D-20-0267.1.

Capet, X., J. C. McWilliams, M. J. Molemaker, and A. F. Shchepetkin, 2008: Mesoscale to submesoscale transition in the California Current system. Part III: Energy balance and flux. *J. Phys. Oceanogr.*, **38**, 2256–2269, https://doi.org/10.1175/2008JPO3810.1.

Carpenter, J. R., A. Rodrigues, L. K. P. Schultze, L. M. Merckelbach, N. Suzuki, B. Baschek, and L. Umlauf, 2020: Shear instability and turbulence within a submesoscale front following a storm. *Geophys. Res. Lett.*, **47**, e2020GL090365, https://doi.org/10.1029/2020GL090365.

Chen, Z., X. Wang, and L. Liu, 2020: Reconstruction of three-dimensional ocean structure from sea surface data: An application of isQG method in the southwest Indian Ocean. *J. Geophys. Res. Oceans*, **125**, e2020JC016351, https://doi.org/10.1029/2020JC016351.

Chrysagi, E., L. Umlauf, P. Holtermann, K. Klingbeil, and H. Burchard, 2021: High-resolution simulations of submesoscale processes in the Baltic Sea: The role of storm events. *J. Geophys. Res. Oceans*, **126**, e2020JC016411, https://doi.org/10.1029/2020JC016411.

D'Asaro, E. A., C. C. Eriksen, M. D. Levine, C. A. Paulson, P. Niiler, and P. V. Meurs, 1995: Upper-ocean inertial currents forced by a strong storm. Part I: Data and comparisons with linear theory. *J. Phys. Oceanogr.*, **25**, 2909–2936, https://doi.org/10.1175/1520-0485(1995)025<2909:UOICFB>2.0.CO;2.

——, C. Lee, L. Rainville, R. Harcourt, and L. Thomas, 2011: Enhanced turbulence and energy dissipation at ocean fronts. *Science*, **332**, 318–322, https://doi.org/10.1126/science.1201515.

——, and Coauthors, 2018: Ocean convergence and the dispersion of flotsam. *Proc. Natl. Acad. Sci. USA*, **115**, 1162–1167, https://doi.org/10.1073/pnas.1718453115.

Dauhajre, D. P., and J. C. McWilliams, 2018: Diurnal evolution of submesoscale front and filament circulations. *J. Phys. Oceanogr.*, **48**, 2343–2361, https://doi.org/10.1175/JPO-D-18-0143.1.

Dong, J., B. Fox-Kemper, H. Zhang, and C. Dong, 2020: The scale of submesoscale baroclinic instability globally. *J. Phys. Oceanogr.*, **50**, 2649–2667, https://doi.org/10.1175/JPO-D-20-0043.1.

——, ——, ——, and ——, 2021: The scale and activity of symmetric instability estimated from a global submesoscale-permitting ocean model. *J. Phys. Oceanogr.*, **51**, 1655–1670, https://doi.org/10.1175/JPO-D-20-0159.1.

Ferrari, R., and C. Wunsch, 2009: Ocean circulation kinetic energy: Reservoirs, sources, and sinks. *Annu. Rev. Fluid Mech.*, **41**, 253–282, https://doi.org/10.1146/annurev.fluid.40.111406.102139.

Flagg, C. N., G. Schwartze, E. Gottlieb, and T. Rossby, 1998: Operating an acoustic Doppler current profiler aboard a container vessel. *J. Atmos. Oceanic Technol.*, **15**, 257–271, https://doi.org/10.1175/1520-0426(1998)015<0257:OAADCP>2.0.CO;2.

Forget, G., J.-M. Campin, P. Heimbach, C. N. Hill, R. M. Ponte, and C. Wunsch, 2015: ECCO version 4: An integrated framework for non-linear inverse modeling and global ocean state estimation. *Geosci. Model Dev.*, **8**, 3071, https://doi.org/10.5194/gmd-8-3071-2015.

Forryan, A., A. C. Naveira Garabato, K. L. Polzin, and S. Waterman, 2015: Rapid injection of near-inertial shear into the stratified upper ocean at an Antarctic Circumpolar Current front. *Geophys. Res. Lett.*, **42**, 3431–3441, https://doi.org/10.1002/2015GL063494.

Fox-Kemper, B., R. Ferrari, and R. Hallberg, 2008: Parameterization of mixed layer eddies. Part I: Theory and diagnosis. *J. Phys. Oceanogr.*, **38**, 1145–1165, https://doi.org/10.1175/2007JPO3792.1.

——, and Coauthors, 2011: Parameterization of mixed layer eddies. III: Implementation and impact in global ocean climate simulations. *Ocean Modell.*, **39**, 61–78, https://doi.org/10.1016/j.ocemod.2010.09.002.

Gill, A. E., 1982: *Atmospheric-Ocean Dynamics*. International Geophysics Series, Vol. 30, Academic Press, 662 pp., https://doi.org/10.1016/S0074-6142(08)X6002-4.

Gula, J., M. Molemaker, and J. C. McWilliams, 2014: Submesoscale cold filaments in the Gulf Stream. *J. Phys. Oceanogr.*, **44**, 2617–2643, https://doi.org/10.1175/JPO-D-14-0029.1.

Jochum, M., B. P. Briegleb, G. Danabasoglu, W. G. Large, N. J. Norton, S. R. Jayne, M. H. Alford, and F. O. Bryan, 2013: The impact of oceanic near-inertial waves on climate. *J. Climate*, **26**, 2833–2844, https://doi.org/10.1175/JCLI-D-12-00181.1.

Klymak, J. M., and Coauthors, 2016: Submesoscale streamers exchange water on the north wall of the Gulf Stream. *Geophys. Res. Lett.*, **43**, 1226–1233, https://doi.org/10.1002/2015GL067152.

McWilliams, J. C., 2016: Submesoscale currents in the ocean. *Proc. Roy. Soc.*, **472A**, 20160117, https://doi.org/10.1098/rspa.2016.0117.

——, 2017: Submesoscale surface fronts and filaments: Secondary circulation, buoyancy flux, and frontogenesis. *J. Fluid Mech.*, **823**, 391–432, https://doi.org/10.1017/jfm.2017.294.

Mensa, J. A., Z. Garraffo, A. Griffa, T. M. Özgökmen, A. Haza, and M. Veneziani, 2013: Seasonality of the submesoscale dynamics in the Gulf Stream region. *Ocean Dyn.*, **63**, 923–941, https://doi.org/10.1007/s10236-013-0633-1.

Morrow, R., and P.-Y. Le Traon, 2012: Recent advances in observing mesoscale ocean dynamics with satellite altimetry. *Adv. Space Res.*, **50**, 1062–1076, https://doi.org/10.1016/j.asr.2011.09.033.

——, and Coauthors, 2019: Global observations of fine-scale ocean surface topography with the Surface Water and Ocean Topography (SWOT) mission. *Front. Mar. Sci.*, **6**, 232, https://doi.org/10.3389/fmars.2019.00232.

Müller, M., B. K. Arbic, J. G. Richman, J. F. Shriver, E. L. Kunze, R. B. Scott, A. J. Wallcraft, and L. Zamudio, 2015: Toward an internal gravity wave spectrum in global ocean models. *Geophys. Res. Lett.*, **42**, 3474–3481, https://doi.org/10.1002/2015GL063365.

Munk, W. H., 1981: Internal waves and small-scale processes. *Evolution of Physical Oceanography*, B. A. Warren and C. Wunsch, Eds., MIT Press, 264–291.

Pearson, B., and B. Fox-Kemper, 2018: Log-normal turbulence dissipation in global ocean models. *Phys. Rev. Lett.*, **120**, 094501, https://doi.org/10.1103/PhysRevLett.120.094501.

Pearson, J., and Coauthors, 2020: Biases in structure functions from observations of submesoscale flows. *J. Geophys. Res. Oceans*, **125**, e2019JC015769, https://doi.org/10.1029/2019JC015769.

Qiu, B., S. Chen, P. Klein, C. Ubelmann, L.-L. Fu, and H. Sasaki, 2016: Reconstructability of three-dimensional upper-ocean circulation from SWOT sea surface height measurements. *J. Phys. Oceanogr.*, **46**, 947–963, https://doi.org/10.1175/JPO-D-15-0188.1.

——, T. Nakano, S. Chen, and P. Klein, 2017: Submesoscale transition from geostrophic flows to internal waves in the northwestern Pacific upper ocean. *Nat. Commun.*, **8**, 14055, https://doi.org/10.1038/ncomms14055.

——, S. Chen, P. Klein, J. Wang, H. Torres, L.-L. Fu, and D. Menemenlis, 2018: Seasonality in transition scale from balanced to unbalanced motions in the world ocean. *J. Phys. Oceanogr.*, **48**, 591–605, https://doi.org/10.1175/JPO-D-17-0169.1.

Rocha, C. B., T. K. Chereskin, S. T. Gille, and D. Menemenlis, 2016a: Mesoscale to submesoscale wavenumber spectra in Drake Passage. *J. Phys. Oceanogr.*, **46**, 601–620, https://doi.org/10.1175/JPO-D-15-0087.1.

——, S. T. Gille, T. K. Chereskin, and D. Menemenlis, 2016b: Seasonality of submesoscale dynamics in the Kuroshio Extension. *Geophys. Res. Lett.*, **43**, 11 304–11 311, https://doi.org/10.1002/2016GL071349.

Rossby, T., C. N. Flagg, K. A. Donohue, A. Sanchez-Franks, and J. Lillibridge, 2014: On the long-term stability of Gulf Stream transport based on 20 years of direct measurements. *Geophys. Res. Lett.*, **41**, 114–120, https://doi.org/10.1002/2013GL058636.

Sasaki, H., P. Klein, B. Qiu, and Y. Sasai, 2014: Impact of oceanic-scale interactions on the seasonal modulation of ocean dynamics by the atmosphere. *Nat. Commun.*, **5**, 5636, https://doi.org/10.1038/ncomms6636.

Savage, A. C., and Coauthors, 2017: Spectral decomposition of internal gravity wave sea surface height in global models. *J. Geophys. Res. Oceans*, **122**, 7803–7821, https://doi.org/10.1002/2017JC013009.

Simmons, H. L., and M. H. Alford, 2012: Simulating the long-range swell of internal waves generated by ocean storms. *Oceanography*, **25**, 30–41, https://doi.org/10.5670/oceanog.2012.39.

Su, Z., J. Wang, P. Klein, A. Thompson, and D. Menemenlis, 2018: Ocean submesoscales as a key component of the global heat budget. *Nat. Commun.*, **9**, 775, https://doi.org/10.1038/s41467-018-02983-w.

——, H. Torres, P. Klein, A. F. Thompson, L. Siegelman, J. Wang, D. Menemenlis, and C. Hill, 2020: High-frequency submesoscale motions enhance the upward vertical heat transport in the global ocean. *J. Geophys. Res. Oceans*, **125**, e2020JC016544, https://doi.org/10.1029/2020JC016544.

Sun, D., and Coauthors, 2020: Diurnal cycling of submesoscale dynamics: Lagrangian implications in drifter observations and model simulations of the northern Gulf of Mexico. *J. Phys. Oceanogr.*, **50**, 1605–1623, https://doi.org/10.1175/JPO-D-19-0241.1.

Thomas, L., A. Tandon, and A. Mahadevan, 2008: Submesoscale processes and dynamics. *Ocean Modeling in an Eddying Regime, Geophys. Monogr.*, Vol. 177, Amer. Geophys. Union, 17–38.

Torres, H. S., P. Klein, D. Menemenlis, B. Qiu, Z. Su, J. Wang, S. Chen, and L.-L. Fu, 2018: Partitioning ocean motions into

balanced motions and internal gravity waves: A modeling study in anticipation of future space missions. *J. Geophys. Res. Oceans*, **123**, 8084–8105, https://doi.org/10.1029/2018JC014438.

——, and Coauthors, 2022: Separating energetic internal gravity waves and small-scale frontal dynamics. *Geophys. Res. Lett.*, **49**, e2021GL096249, https://doi.org/10.1029/2021GL096249.

Tsujino, H., and Coauthors, 2020: Evaluation of global ocean–sea-ice model simulations based on the experimental protocols of the Ocean Model Intercomparison Project phase 2 (OMIP-2). *Geosci. Model Dev.*, **13**, 3643–3708, https://doi.org/10.5194/gmd-13-3643-2020.

Uchida, T., R. Abernathey, and S. Smith, 2017: Seasonality of eddy kinetic energy in an eddy permitting global climate model. *Ocean Modell.*, **118**, 41–58, https://doi.org/10.1016/j.ocemod.2017.08.006.

——, and Coauthors, 2022: Cloud-based framework for inter-comparing submesoscale permitting realistic ocean models. *Geosci. Model Dev.*, **15**, 5829–5856, https://doi.org/10.5194/gmd-15-5829-2022.

Wang, D.-P., C. N. Flagg, K. Donohue, and H. T. Rossby, 2010: Wavenumber spectrum in the Gulf Stream from shipboard ADCP observations and comparison with altimetry measurements. *J. Phys. Oceanogr.*, **40**, 840–844, https://doi.org/10.1175/2009JPO4330.1.

Zhai, X., R. J. Greatbatch, and J.-D. Kohlmann, 2008: On the seasonal variability of eddy kinetic energy in the Gulf Stream region. *Geophys. Res. Lett.*, **35**, L24609, https://doi.org/10.1029/2008GL036412.

Zhang, Z., Y. Zhang, B. Qiu, H. Sasaki, Z. Sun, X. Zhang, W. Zhao, and J. Tian, 2020: Spatiotemporal characteristics and generation mechanisms of sub-mesoscale currents in the northeastern South China Sea revealed by numerical simulations. *J. Geophys. Res. Oceans*, **125**, e2019JC015404, https://doi.org/10.1029/2019JC015404.